Editors' Suggestion

Changes of Fermi surface topology due to the rhombohedral distortion in SnTe

Christopher D. O'Neill,[1,*] Oliver J. Clark,[2] Harry D. J. Keen,[1] Federico Mazzola,[2] Igor Marković,[2,3] Dmitry A. Sokolov,[3] Andreas Malekos,[1] Phil D. C. King,[2] Andreas Hermann,[1] and Andrew D. Huxley[1]

[1]*Centre for Science at Extreme Conditions and SUPA, School of Physics and Astronomy, University of Edinburgh, Edinburgh EH9 3JZ, United Kingdom*

[2]*School of Physics and Astronomy, University of St Andrews, St Andrews KY16 9SS, United Kingdom*

[3]*Max Planck Institute for Chemical Physics of Solids, Nöthnitzer Straße 40, 01187 Dresden, Germany*

(Received 3 July 2020; accepted 29 September 2020; published 21 October 2020)

Stoichiometric SnTe is theoretically a small gap semiconductor that undergoes a ferroelectric distortion on cooling. In reality however, crystals are always nonstoichiometric and metallic; the ferroelectric transition is therefore, more accurately described as a polar structural transition. Here, we study the Fermi surface using quantum oscillations as a function of pressure. We find the oscillation spectrum changes at high pressure due to the suppression of the polar transition and less than 10 kbars is sufficient to stabilize the undistorted cubic lattice, this is accompanied by a large decrease in the Hall and electrical resistivities. Combined with our density functional theory calculations and angle-resolved photoemission spectroscopy measurements, this suggests the Fermi surface L pockets have lower mobility than the tubular Fermi surfaces that connect them. Additionally, we find the unusual phenomenon of a linear magnetoresistance that exists irrespective of the distortion that we attribute to regions of the Fermi surface with high curvature.

DOI: 10.1103/PhysRevB.102.155132

I. INTRODUCTION

On first appearance, SnTe looks like a simple semiconductor with a small band gap that is formed by the ionic transfer between Sn and Te. Despite its simplicity, SnTe is known to host several interesting phenomena including ferroelectricity [1,2] and is a topological crystalline insulator with potential surface states [3,4]. Grown samples are, however, always nonstoichiometric and Te rich with the Sn deficiency accommodated in the lattice as vacancies [5]. As a consequence, the Fermi level is shifted into the valence band, leading to metallic behavior with a free carrier concentration of holes n_h. The polar state transition temperature T_c is below 100 K and n_h dependent [6]. Increasing n_h reduces T_c and eventually stabilizes the undistorted lattice. Although avoiding the polar distortion is advantageous for studying topological states which are protected by crystalline symmetry, the large n_h makes any investigation of surface states by transport extremely difficult. So far, there are no reports on how T_c varies under pressure. Here, we use hydrostatic pressure to suppress T_c and measure the associated changes in Fermi surface topology and transport properties.

At 300 K, SnTe has a fcc rocksalt structure shown in Fig. 1(a) with space-group $Fm\bar{3}m$. The polar distortion is driven by a soft transverse optic phonon [1,2], that distorts the lattice along the (111) direction of the cubic structure to a $R3m$ rhombohedral phase with shear angle $\alpha \approx 59.878^\circ$ [7] ($\alpha = 60^\circ$ for fcc) and relative shift of the two fcc sublattices of $\upsilon \sim 0.008$ (~9 pm) [8]. Previous band-structure calculations of the cubic phase show a valence band made up of filled Te orbitals and a conduction band of empty Sn orbitals except at the narrowest gap (1,1,1) L point of the Brillouin zone where a spin-orbit-driven band inversion occurs [3,9]. For small n_h, the cubic Fermi surface is made up of disconnected pockets at the L points. On increasing n_h, the pockets elongate, and above $n_h \sim 1 \times 10^{20}$ cm^{-3}, are joined by tubes [10,11]. Quantum oscillation measurements on bulk crystals resolved three to four frequencies belonging to the L pockets for low values of n_h [12,13]. These merged to a single frequency at increased doping levels where the undistorted lattice is anticipated to be stable at 0 K. The distortion, therefore, clearly has consequences for the Fermi surface topology, that have yet to be fully determined.

Angle-resolved photoemission spectroscopy (ARPES) measurements could not resolve any changes in Fermi surface topology with temperature below T_c, however, they did see a shift in much of the density of states and a widening of the band gap [10]. Although the band gap is a result of ionic transfer between Sn and Te, its widening below T_c suggests the polar transition has an electronic component resembling a Peierls instability. Such a mechanism would, indeed, lead to changes in Fermi surface topology. Recent measurements on thin films also suggest the possibility that the different quantum oscillation frequencies in the rhombohedral phase may be a result of spin splitting by a spin-orbit Rashba mechanism [14].

Avoiding T_c using pressure on a sample with fixed doping provides a unique route to investigate any changes in Fermi surface associated with the distortion. Here, we report that a pressure of 10 kbars is adequate to suppress the distortion in a sample with $T_c = 89$ K at 6 kbars.

*chris.oneill@ed.ac.uk

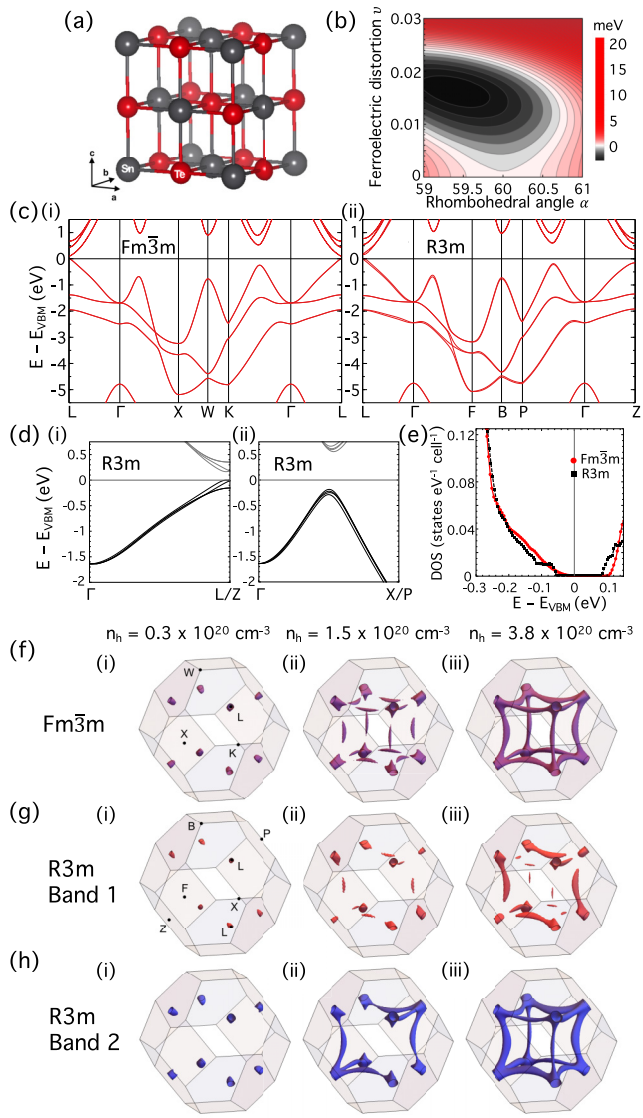

FIG. 1. (a) The cubic structure of SnTe at 300 K. (b) The energetic landscape of the rhombohedral distortion at 0 K. Here, the cubic structure is at zero energy and is a saddle point at $\alpha = 60^\circ$ and $\upsilon = 0$. (c) The electronic band structure of stoichiometric SnTe along equivalent high-symmetry paths in the: (i) $Fm\bar{3}m$ cubic and (ii) $R3m$ rhombohedral structures. Here, the band energy (E) is plotted relative to the valence-band maximum (E_{VBM}). (d) A closeup view of the valence-band dispersion for the $R3m$ structure along directions relevant to the Fermi surface topology. Here, degeneracy has been lifted along both: (i) Γ-L/Z and (ii) Γ-X/P directions as a result of the distortion. (e) The electronic density of states as a function of $E - E_{\mathrm{VBM}}$ for each structure. (f) The evolution of the Fermi surface for the $Fm\bar{3}m$ structure at three positions of the Fermi energy (E_F) with respect to E_{VBM}; (i) -0.165 eV, (ii) -0.282 eV, and (iii) -0.330 eV. Corresponding carrier concentrations n_h are marked in the legend. (g) and (h) The evolution of the Fermi surface for the $R3m$ structure made up of two nondegenerate bands. Here, the E_F shifts downwards to (i) -0.182, (ii) -0.286, and (iii) -0.344 eV, in order to conserve n_h values.

TABLE I. Values of polar transition temperature T_c and corresponding carrier concentration n_h for the three single-crystal samples studied here.

Sample (pressure)	T_c (K)	n_h ($\times 10^{20}$ cm^{-3})
S1 (ambient)	79	2.93 ± 0.15
S2 (ambient)	75	3.09 ± 0.14
S3 (6 kbars)	89	1.12 ± 0.04

II. EXPERIMENT AND RESULTS

Single crystals of SnTe were grown by the same method described elsewhere [2] with high-purity elements Sn (99.9999%) and Te (99.9999%) in a ratio 51:49 to minimize n_h. Crystals had natural facet faces along cubic axes and were orientated by Laue x-ray diffraction. The T_c and n_h of the crystals was determined from their electrical resistivity and Hall effect, respectively. A list of the samples studied along with their T_c and n_h is given in Table I (S3 was used in pressure studies). The values of T_c are in close agreement with previous reports for samples with similar n_h at ambient pressure in Ref. [6].

ARPES measurements were performed on sample S1 at the CASSIOPEE beamline of Synchrotron SOLEIL using a Scienta R4000 hemispherical analyzer with a vertical entrance slit and light incident in the horizontal plane. The sample was cleaved *in situ* and measured at temperatures below 15 K. Measurements were taken with p-polarized light at photon energies of 110 and 135 eV. The approximate positions in k_z of k_x-k_y Fermi surface contours and band dispersions were determined from the experimentally observed periodicity of band features as a function of photon energy in conjunction with reference density functional theory calculations.

Samples S2 and S3 were cut by spark erosion into blocks with [001] cubic axes along the length, width and height and had dimensions $1.80 \times 0.45 \times 0.32$ mm and $175 \times 115 \times 100$ μm, respectively. Gold electrical contacts were attached by spot welding and resistivity (ρ), Hall effect and magnetoresistance (MR) measurements made with a current of 100 μA at 37 Hz. Experiments were carried out in a ^{4}He cryostat with a 9-T Cryogenic Ltd. magnet and a dilution refrigerator with 15-T Oxford Instruments magnet. Sample S2 was used to study quantum oscillations as a function of applied field angle with a rotating sample stage. Sample S3 was studied under pressure. Pressure was applied in a diamond-anvil pressure cell that had diamond culets of 800 μm in diameter. Daphne oil 7373 was used as the pressure transmitting medium. A preindented steel gasket with a 300-μm hole, insulated with a Al_2O_3 and Stycast 1266 epoxy mixture, contained the sample under pressure. The pressure was determined via fluorescence lines of a small ruby chip at 300 K.

Fully relativistic density-functional theory calculations were carried out for stoichiometric SnTe with the VASP package and the Perdew-Burke-Ernzerhof exchange-correlation functional [15–17] for a plane-wave basis with cutoff energy $E_c = 240$ eV and k-point sampling with a linear density of $60/\text{Å}^{-1}$ ($30/\text{Å}^{-1}$ for mapping the potential-energy surface). Constant-pressure structure optimizations were performed un-

til remaining force components were less than 1 meV/Å. We found the ground-state energy for the rhombohedral structure to be ∼2 meV/unit lower than the cubic structure with a rhombohedral angle distortion of $\alpha \approx 59.66^\circ$ and polar displacement of $\upsilon \approx 0.012$, somewhat larger than found in previous scalar relativistic calculations [2]. The potential-energy surface for the distortion is shown in Fig. 1(b). These values closely resemble those seen by x-ray and neutron scattering ($\alpha \approx 59.878^\circ$ and $\upsilon = 0.007$ for $n_h = 1.0$ and 0.88×10^{20} cm^{-3}, respectively) [7,8]. The calculated band structure in the $Fm\bar{3}m$ cubic phase is shown in Fig. 1(c)(i) where the smallest band gap is seen at the L point as expected. An analysis of band character (not shown here) confirms the expected band inversion at this point [3,9]. The evolution of the Fermi surface with hole doping, within the frozen band approximation for this structure, is shown in Fig. 1(f) with the Fermi energy (E_F) at (i) −0.165 eV ($n_h = 0.3 \times 10^{20}$ cm^{-3}), (ii) −0.282 eV ($n_h = 1.5 \times 10^{20}$ cm^{-3}), and (iii) −0.330 eV ($n_h = 3.8 \times 10^{20}$ cm^{-3}) with respect to the top of the valence band. Below ~ -0.25 eV (above $n_h \sim 1 \times 10^{20}$ cm^{-3}) the band along Γ-K crosses E_F and ultimately leads to tubes connecting the L pockets.

The electronic band structure for the $R3m$ rhombohedral structure is shown in Fig. 1(c)(ii). Whether the band inversion survives into the $R3m$ phase depends on the size of the distortion, consistent with previous studies [18]. Additionally, the breaking of cubic symmetry lifts degeneracies throughout the Brillouin zone. The paths relevant to the Fermi surface topology are Γ-L/Z and Γ-X/P (Γ-L and Γ-K in cubic notation), shown in Figs. 1(d)(i) and 1(d)(ii), respectively. The resulting Fermi surface, now, consists of hole pockets from two nondegenerate bands shown in Figs. 1(g) and 1(h). The single eightfold degenerate L pockets from the cubic phase is split into four unique pockets, two per band. This is a consequence of both rhombohedral symmetry breaking and spin-orbit splitting to lift the band degeneracy. The total carrier concentration (Fermi surface volume) must remain constant between the two phases. Hence, the $R3m$ phase sees a downward shift of E_F to (i) −0.182 eV, (ii) −0.286 eV, and (iii) −0.344 eV for the equivalent carrier concentrations in Fig. 1(f). The density of states for the $Fm\bar{3}m$ and $R3m$ structures is shown in Fig. 1(e). For the $R3m$ structure, the density of states does not resolve some of the subtle features very close to the valence-band maximum that are extremely small in volume. These small features contribute a negligible number of carriers to the computed n_h. Additionally, the positions of the Fermi level considered, here, are well below these parts of the band structure.

ARPES measurements, performed with photon energies of $h\nu = 135$ and 110 eV, chosen to approximately probe planes which pass through the center and the L/Z points of the Brillouin zone, respectively, are shown in Fig. 2. The measured band dispersions along X/P-Γ-X/P directions [Fig. 2(a)] show the three Te p-derived bands found from DFT. Although the measurements were performed at 15 K, in the rhombohedral phase, it is not possible to identify signatures of the band splittings which result from the breaking of cubic symmetry or the small differences between the dispersions along the Γ-X and Γ-P directions. This is likely predominantly due to large intrinsic k_z broadening in our measurements, which is a result of the surface sensitivity of photoemission. Other contributions to resolving the distortion include the energy (25 meV at 110 eV and 35 meV at 135 eV) and angular resolution ($\approx 0.3^\circ$) of the experimental setup.

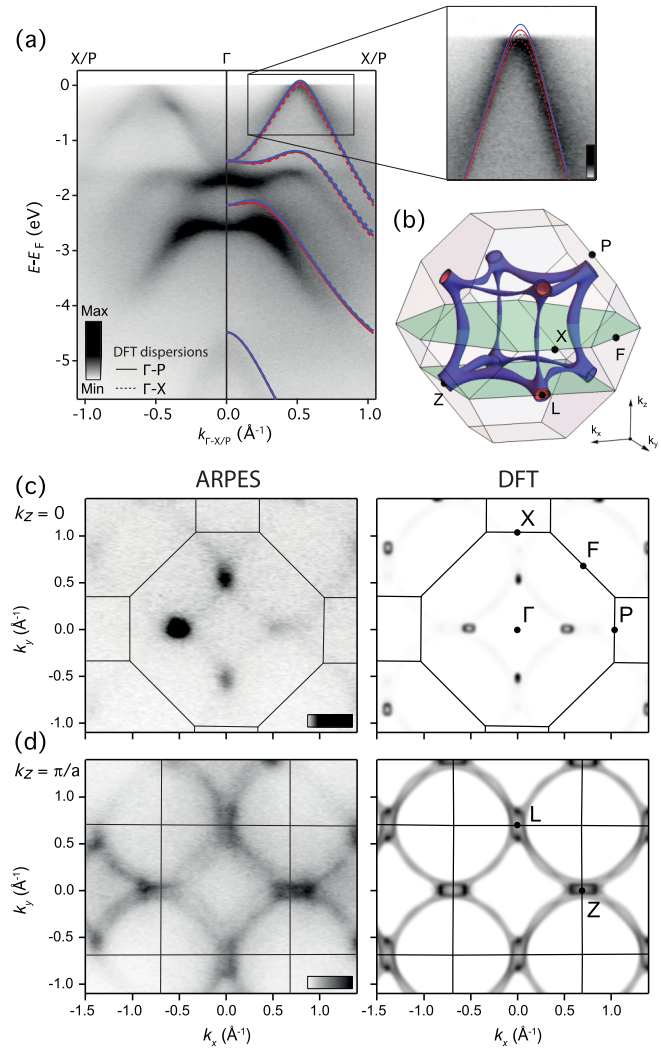

FIG. 2. (a) ARPES band dispersions along the X/P-Γ-X/P direction measured with $h\nu = 135$ eV light (gray scale). Density functional theory (DFT) calculations for the $R3m$ structure, shifted in energy by 0.324 eV, are included as overlays (lines). (b) Three-dimensional schematic of the $R3m$ Brillouin zone with the calculated Fermi surface for a Fermi energy (E_F) of −0.324 eV with respect to the valence-band maximum. Shaded planes at $k_z = 0$ and $-\frac{\pi}{a}$ indicate the positions of extracted k_x-k_y contours in (c) and (d), respectively. (c) and (d) Fermi surface contours obtained with ARPES at $E_F \pm 25$ meV collected using $h\nu = 135$ and 110 eV photons to approximate the $k_z = 0$ and $k_z = \pi/a$ contours, respectively, and simulated DFT images for the Fermi surface in (b). The simulated DFT ARPES images were produced with a set of 600 planes along k_z between ±2.4 Å^{-1}, centered on the plane of interest. The contour was generated from the intersection of each plane with the Fermi surface and is realistically blurred to simulate the finite effective energy and k_x-k_y resolutions in experiment. Finally, all planes were summed up and weighted with a Lorentzian to simulate k_z broadening. The $R3m$ Brillouin zone boundary is overlaid as a guide and high-symmetry points are labeled.

Nonetheless, comparison with the calculations is instructive. In particular, we find that the valence bands just cut the Fermi level along the Γ-X/P direction. This indicates a doping level such that the L points are connected by tubular Fermi surfaces [Fig. 2(b)]. Consistent with this, we show in Figs. 2(c) and 2(d) ARPES Fermi surface measurements corresponding to the planes shown in Fig. 2(b). These are compared with simulated spectra from our DFT calculations, performed for a Fermi level 0.324 eV below the valence-band maximum (corresponding to a calculated hole density $n_h = 2.8 \times 10^{20}$ cm^{-3}, close to the value from Hall effect measurements in Table I). The bands forming the tubelike regions are directly visible on a plane encompassing the L points of the Brillouin zone [Fig. 2(d)], whereas the cross sections of these tubular sections is apparent in the Fermi surface measured on the $k_z = 0$ plane [Fig. 2(c)].

Resistivity for sample S2 normalized to the value at 300 K ($\rho_{300\,\mathrm{K}}$) is shown in Fig. 3(a). An anomaly due to the increased electron-soft phonon scattering exists at T_c [19], made clearer by differentiation (T_c and n_h are listed in Table I). The MR $= [\rho(B) - \rho(0)]/\rho(0)$, up to $B = 15$ T at 40 mK for a series of applied field angles θ is shown in Fig. 3(b). Here, $\theta = 0$ corresponds to $B \parallel [001]$. Rotation was in increments of 5° to $B \parallel [011]$ at $\theta = 45°$ through to the $B \parallel [010]$ axis at $\theta = 90°$. Shubnikov–de Haas quantum oscillations (SdH) exist above 8 T and were extracted by subtracting a smoothly varying polynomial background. Examples of the SdH against B^{-1} for $\theta = 0°$ and $\theta = 45°$ are shown in Fig. 3(c) and contain a beating pattern characteristic of several neighboring frequencies. Fast Fourier transforms (FFT) resolved three to four distinct oscillation frequencies that are labeled β_1-β_4 in Fig. 3(d). The angular dependence of the oscillation frequencies F is shown in Fig. 3(e). The lowest-frequency β_1 follows:

$$F(\gamma) = \frac{F(0)}{\sqrt{\cos^2\gamma + \frac{1}{\epsilon}\sin^2\gamma}} \qquad (1)$$

expected for an ellipsoid with eccentricity ϵ, shown as the black dashed line. Here, γ is the angle with respect to the principal axis of the ellipsoid ([1,1,1] direction). Frequencies β_2-β_4 clearly contain more structure than can be explained by a simple ellipsoid.

A contour plot of the FFT spectra normalized to the largest peak amplitude as a function of frequency and angle is shown in Fig. 3(f). Also included are the calculated frequencies for the L pockets of both $R3m$ Fermi surface bands with $n_h = 2.7 \times 10^{20}$ cm^{-3} and a distortion of $\alpha = 59.86°$ and $\upsilon = 0.006$. These values of n_h, α and υ give excellent agreement between experimental results and calculation in Fig. 3(f). The Fermi surfaces are shown in Fig. 3(g). The α and υ values were determined by how the oscillation frequencies vary as a function of the rhombohedral distortion. For this, we constructed a set of linearly interpolated crystal structures between the cubic $Fm\bar{3}m$ and the optimized $R3m$ structures ($\alpha = 59.66°$ and $\upsilon = 0.012$). The change in frequencies for the L pockets with $B \parallel [001]$ as a function of

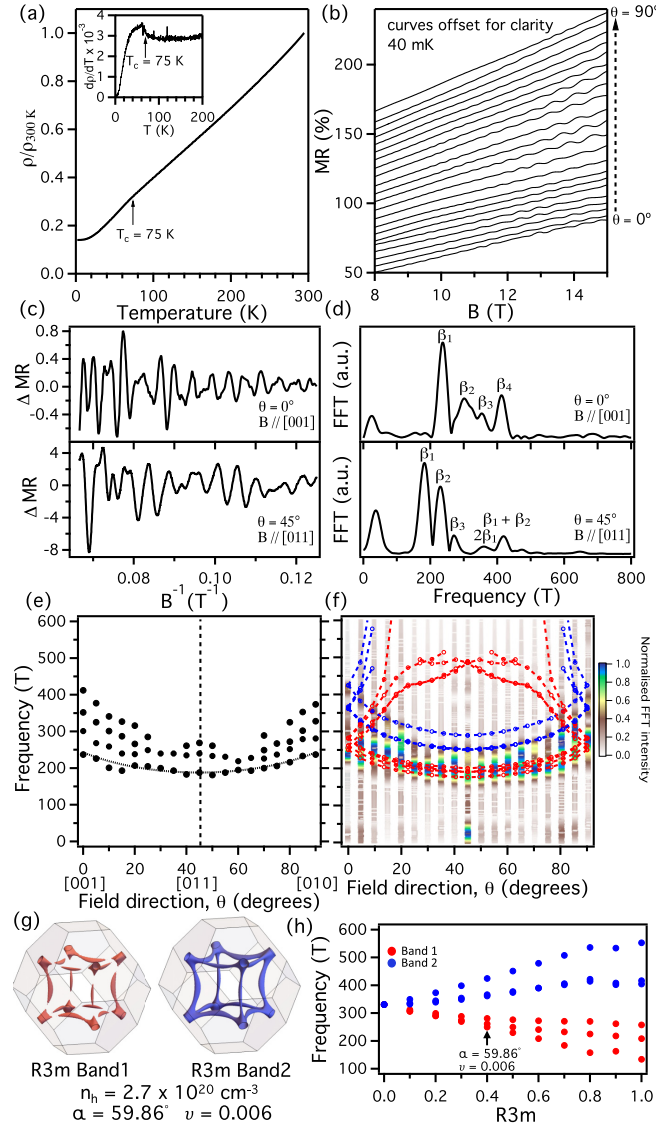

FIG. 3. (a) The resistivity ρ normalized to the value at 300 K for sample S2. The anomaly at $T_c = 75$ K is made clearer by differentiation (inset). (b) The MR $= [\rho(B) - \rho(0)]/\rho(0)$ at 40 mK for a series of applied field angles θ. Curves have been offset for clarity. Above 8 T, Shubnikov–de Haas oscillations exist. (c) Examples of the oscillations plotted against the inverse field for $\theta = 0°$ ($B \parallel [001]$) and $\theta = 45°$ ($B \parallel [011]$). (d) FFTs of (c), where three to four distinct frequencies labeled β_1-β_4 are resolved. (e) The evolution of β_1-β_4, shown as markers, as a function of θ. The black dashed line corresponds to an ellipse given by Eq. (1) with an eccentricity of $\epsilon = 5$. (f) A color scale of the FFT amplitude normalized to the maximum value as a function of field angle and frequency. Red (band 1) and blue (band 2) markers with dashed lines are the expected oscillation frequencies for the pockets at L in the $R3m$ calculated Fermi surfaces in (g) where $n_h = 2.7 \times 10^{20}$ cm^{-3} and the distortion is $\alpha = 59.86°$ and $\upsilon = 0.006$. (h) Shows the calculated oscillation frequencies for the pockets at L with $B \parallel [001]$ as a function of the distortion size. Here, 0 is the $Fm\bar{3}m$ structure, and 1 is the $R3m$ distortion that minimizes the DFT energy. The actual distortion is taken to be the value at the arrow.

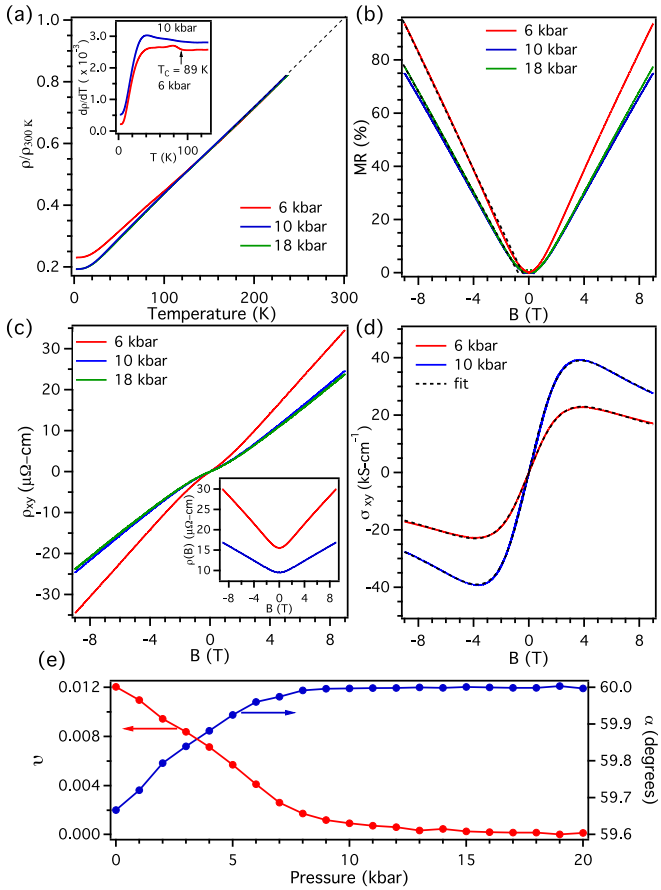

FIG. 4. (a) The resistivity ρ of sample S3 normalized to the value at 300 K for pressures 6, 10, and 18 kbars. Here, the high-temperature freezing of Daphne oil is avoided by extrapolation (dashed line). The inset $d\rho/dT$ gives $T_c = 89$ K at 6 kbars. No anomaly due to T_c can be identified at 10 kbars. (b) The MR at 2 K with $B \parallel [001]$ for the above pressures. The black dashed lines are straight line fits between 1 and 9 T. (c) The Hall resistivity ρ_{xy}. The insets are the corresponding curves of $\rho(B)$ with no normalization. (d) The Hall conductivity σ_{xy} at 6 and 10 kbars. Fits to Eq. (5) are shown as black dashed lines. (e) Pressure dependence of polar displacement υ (left axis) and the rhombohedral angle α (right axis) as a function of pressure from spin-orbit coupling DFT calculations.

distortion is in Fig. 3(h). This illustrates the substantial effect of the rhombohedral distortion on Fermi surface topology.

Resistivity curves normalized to $\rho_{300\,\mathrm{K}}$ for sample S3 studied under pressure are in Fig. 4(a) with the $d\rho/dT$ inset. Here, $\rho_{300\,\mathrm{K}}$ was determined by extrapolation (black dashed line) to avoid a high-temperature anomaly where the Daphne oil freezes. At 6 kbars, $d\rho/dT$ gives $T_c = 89$ K. On increasing pressure to 10 kbars, no anomaly in $d\rho/dT$ can be identified. There is also a sharp drop in $\rho/\rho_{300\,\mathrm{K}}$ by a factor of 1.58 at 2 K. No further changes were observed at 18 kbars, and the curve is almost indistinguishable from that at 10 kbars. The magnetoresistance and Hall resistivity ρ_{xy} at 2 K are shown in Figs. 4(b) and 4(c), respectively. The Hall conductivity σ_{xy} is given by

$$\sigma_{xy} = \frac{\rho_{xy}}{\{\rho(B)\}^2 + \rho_{xy}^2}, \tag{2}$$

and is shown in Fig. 4(d).

The Hall resistivity and magnetoresistance measured on sample S3 up to 14 T at 40 mK are shown in Figs. 5(a) and 5(b). Both quantities contain SdH oscillations above 8 T. Here, only measurements with $B \parallel [001]$ could be taken. Figure 5(c) shows the SdH against B^{-1} for 6 kbars in: (i) the Hall effect and (ii) the MR and for 10 kbars in (iii) the Hall effect and (iv) the MR. The FFT in Fig. 5(d) shows three frequencies exist in both the Hall and the MR at 6 kbars; $\beta_1 = 209$, $\beta_2 = 246$, and $\beta_3 = 290$ T. Only a single frequency in the FFT at $\beta = 198$ T exists at 10 kbars in Fig. 5(d) for both the Hall and the MR.

The temperature dependence of the quantum oscillation amplitude is governed by the temperature reduction term R_T in the Lifshitz-Kosevich formula given by

$$R_T = \frac{\kappa m^* T/B}{\sinh(\kappa m^* T/B)}, \tag{3}$$

where $\kappa = 2\pi^2 k_B/e\hbar$ and m^* is the effective mass. The SdH amplitude normalized to the value at 40 mK with corresponding fits to R_T are shown in Fig. 5(e). Measurements were limited to 3 K, the maximum temperature of the dilution refrigerator where only a slight decrease in amplitude could be realized. Derived effective masses for β_1-β_3 are the same within error with an average value of $m^* = 0.171 \pm 0.012 m_e$. At 10 kbars, no change in m^* was seen within error for β and $m^* = 0.165 \pm 0.011 m_e$.

The quantum oscillation amplitude dependence on field is determined by the Dingle term R_D in the Lifshitz-Kosevich formula given by

$$R_D = \exp\left(\frac{-\kappa m^* T_D}{B}\right), \tag{4}$$

where the Dingle temperature $T_D = \hbar/2\pi k_B \tau$ can be used to calculate the scattering time τ. Beating patterns at 6 kbars make any estimate of T_D highly uncertain. At 10 kbars, a graph of $\ln[AB^{1/2}\sinh(\kappa m^* T/B)]$ against B^{-1} is shown in Fig. 5(f), where A is the oscillation amplitude. A straight line fit gives $T_D = 15.7 \pm 1.1$ K and, consequently, $\tau = 7.76 \pm 0.55 \times 10^{-14}$ s. The solid red line in Fig. 5(c) is a calculation with $T_D = 15.7$ K for a single oscillation frequency of 198 T, showing excellent agreement with the measurements.

III. DISCUSSION

Having presented our theoretical and experimental findings, we now discuss the significance of the results. DFT band-structure calculations highlight the large changes in Fermi surface topology as a consequence of the polar distortion. The qualitative agreement with our ARPES measurements reported here provides a validation in the accuracy of our DFT calculations close to the Fermi surface and confirms that the off-stoichiometry leads to a degenerate doping, i.e., the Fermi level shifts into the valence bands.

Quantum oscillations below T_c contain three to four neighboring frequencies. The DFT calculation identifies the detected oscillations to be from the L pockets that have a similar angular dispersion, even when these pockets are connected by tubelike Fermi surfaces. The expected oscillation frequencies for the connecting tubes are all less than 80 T for the Fermi surface in Fig. 3(g) and were not resolved in

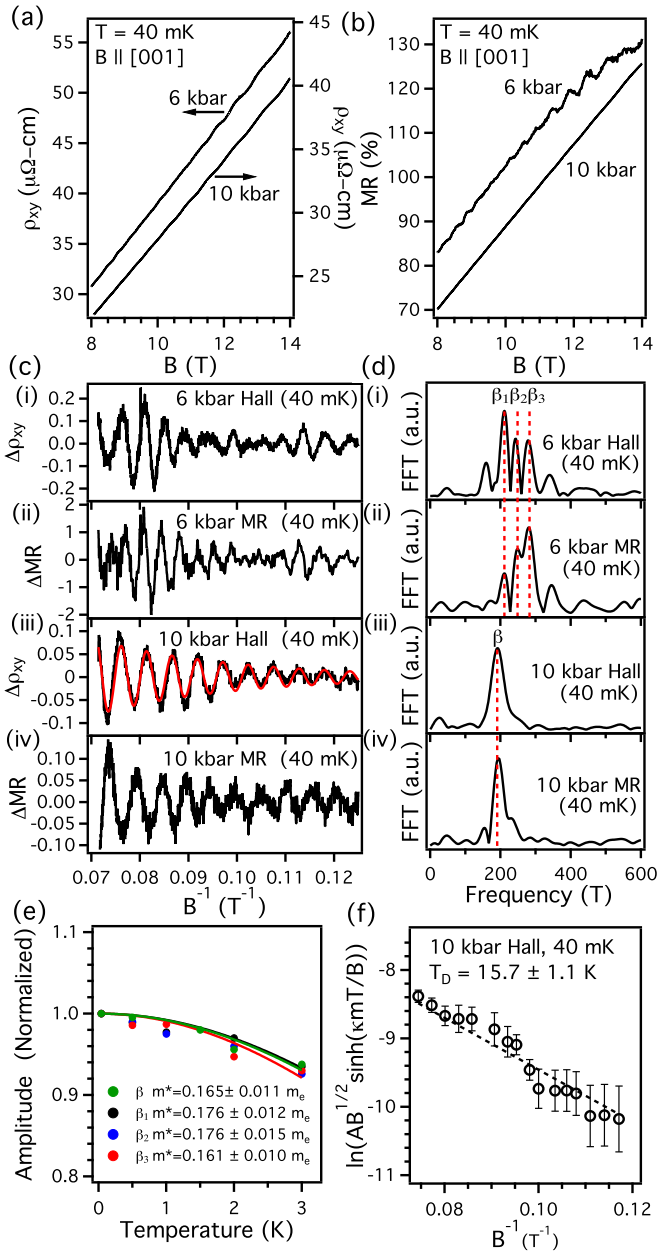

FIG. 5. (a) The Hall resistivity ρ_{xy} at 40 mK with $B \parallel [001]$ for 6 kbars (left axis) and 10 kbars (right axis). (b) The corresponding MR at 6 and 10 kbars. Shubnikov–de Haas oscillations exist above 8 T in both ρ_{xy} and MR. (c) The oscillations against B^{-1} in: (i) ρ_{xy}, (ii) the MR for 6 kbars, (iii) ρ_{xy}, and (iv) the MR for 10 kbars. (d) (i)–(iv) The associated fast Fourier transforms of the oscillations in (c). At 6 kbars in (i) and (ii) three frequencies marked β_1-β_3 exist in both ρ_{xy} and MR. A single frequency $\beta = 198$ T exists for 10 kbars in (iii) and (iv). (e) The oscillation amplitude in ρ_{xy} against temperature, normalized to the value at 40 mK, for β_1-β_3 at 6 kbars and β at 10 kbars. Solid lines are fits to Eq. (3) that give the calculated effective masses given in the legend. (f) The Dingle plot of the β oscillation amplitude at 10 kbars in ρ_{xy} at 40 mK. Here, a straight line fit gives $T_D = 15.7 \pm 1.1$ K. For verification, the solid red line in (c)(iii) corresponds to an oscillation with frequency 198 T and amplitude given by Eq. (4) with $T_D = 15.7$ K.

TABLE II. The values of carrier concentration n_h and mobility μ_h in sample S3 according to the fits of σ_{xy} in Fig. 4(d).

	$R3m$ (6 kbars)	$Fm\bar{3}m$ (10 kbars)
n_h ($\times 10^{20}$ cm^{-3})	1.12 ± 0.04	1.83 ± 0.05
μ_h (cm^2 V^{-1} s^{-1})	2570 ± 50	2660 ± 50

experiment. Although peaks exist at ≈30 T in the FFT spectra, they may also be a result of subtracting the polynomial background. There are four unique L pockets that vary in size in the rhombohedral phase as a consequence of rhombohedral symmetry breaking and spin-orbit splitting lifting the band degeneracy. The presence of several neighboring oscillation frequencies for $B \parallel [001]$ is, therefore, expected in the $R3m$ structure [Fig. 3(h)]. This is consistent with previous studies [14]. In the cubic phase, the single eightfold degenerate L pockets are expected to give only a single oscillation frequency for $B \parallel [001]$. With pressure, we find 10 kbars is adequate to merge the neighboring frequencies into a single frequency. Additionally, at 10 kbars, no anomaly in resistivity due to T_c can be identified. Therefore, the rhombohedral transition has been suppressed by a pressure of 10 kbars. This is also accurately captured in DFT calculation, shown in Fig. 4(e) for υ and α as a function of pressure.

The suppression of the rhombohedral transition leads to large changes in Hall signal. ρ_{xy} shows nonlinear behavior for all pressures. Our measurements for σ_{xy} at all pressures are well described by a single band model,

$$\sigma_{xy} = eB\left(\frac{n_h\mu_h^2}{1+\mu_h^2B^2}\right) = \frac{\sigma\omega_c\tau}{1+\omega_c^2\tau^2}, \tag{5}$$

where μ_h is the carrier mobility, σ is the zero-field conductivity, and ω_c is the cyclotron frequency. Equation (5) highlights that, for sufficiently mobile carriers with $\mu_h B \sim 1$, nonlinearity may still exist for a single band. Using a two-band model did not improve the fit despite adding two extra fitting parameters. Values of n_h and μ_h extracted from the fits are given in Table II. Upon entering the cubic phase, the carrier concentration increases significantly by a factor of 1.64, whereas the mobility stays approximately constant within error, consistent with the drop in resistivity by a factor of 1.58.

On increasing pressure in the cubic structure (to 18 kbars), no further changes are observed in any measured quantity. The changes in ρ_{xy} and σ_{xy} are, therefore, a direct consequence of the modification in Fermi surface associated with the distortion. Expected quantum oscillation frequencies from calculations show the distortion acts to increase the volume of some L pockets while decreasing others [Fig. 3(h)]. This is not seen in experiment. Figure 5(d) shows β_1-β_3 at 6 kbars are all larger in magnitude than β at 10 kbars. A full angular dependence is required to say definitively how the pockets change. However, these results point towards the L pockets being smaller in the cubic phase with potentially more carriers in the connecting tubes to maintain a fixed total number of carriers.

Quantum oscillations at 10 kbars give $\mu_h = e\tau/m^* = 846 \pm 59$ cm^2 V^{-1} s^{-1}, significantly less than the mobility from the Hall effect in Table II. This suggests that the Hall conductivity is dominated by the connecting tubes that have a significantly higher mobility than the L pockets. Therefore, for the cubic phase, more carriers in the connecting tubes, in turn, lead to more carriers becoming visible to the Hall effect, providing a simple explanation for the changes seen here. Since the Dirac points are not close to E_F, the role of surface contributions can be discounted.

The MR in Fig. 4(b) follows a similar behavior in both structures. It begins quadratically for low B before becoming linear above 1 T to the highest fields, demonstrated by the straight line fits. Linear MR is an unusual phenomenon and both quantum and classical explanations have been proposed. Abrikosov's well-known quantum model gives a linear MR when all carriers occupy the lowest Landau level for a linear electron energy dispersion [20,21]. The linear MR reported in some topological insulators is expected to be associated with similar quantum effects [22]. Previous reports on SnTe thin films with a larger n_h than our samples saw a linear magnetoresistance and attributed it to Dirac surface states dominating the transport as a result of band bending at the substrate/film interface that brings E_F closer to the Dirac points [23]. In our bulk crystals, such band bending is unlikely.

Classically, linear MR from irregular current paths as a result of disorder was described by Parish and Littlewood [24]. Here, our samples have high mobility carriers and quantum oscillations that reflect relatively little disorder, making a Parish-Littlewood mechanism unlikely. Instead, we suggest a straightforward origin first discussed by Pippard based on a Fermi surface containing sharp corners [25].

Pippard demonstrated that, for sufficiently small values of $\omega_c\tau \ll 2\pi$, Fermi surfaces with sharp corners lead to a MR varying as $\omega_c\tau$ rather than $\omega_c^2\tau^2$ [25]. Although the occurrence of infinitely sharp corners is difficult to imagine in reality, Pippard points out regions with suitably sharp curvature and minimal rounding lead to an initial quadratic form at low field followed by linear behavior with increasing field, analogous to the measurements reported here. At 9 T in the cubic phase, $\omega_c\tau \approx 0.6$, satisfying the requirement $\omega_c\tau \ll 2\pi$. We therefore, attribute the linear MR in SnTe to regions of high curvature present in the Fermi surface for both the cubic and the rhombohedral structures, most likely at the necks where L pockets and connecting tubes meet making an almost right angle. Curvature-driven linear MR has previously been reported in materials with partially gapped Fermi surfaces due to density wave order [26,27], proving it as a potential explanation for many other systems.

IV. CONCLUSIONS

In conclusion, we have shown the polar distortion in SnTe is accompanied by a reconstruction of the Fermi surface. Under ambient pressure, both our quantum oscillation and ARPES measurements are well described with DFT calculations. We found that a pressure of just under 10 kbars stablizes the cubic structure in good agreement with the required pressure calculated with DFT. This, consequently, allows the contribution to the Hall effect for each feature of the Fermi surface to be determined. Linear magnetoresistance has been observed in both structures and attributed to the presence of regions with high curvature in the Fermi surface.

The research data supporting this publication can be accessed at the University of Edinburgh's Datashare repository [28].

ACKNOWLEDGMENTS

We wish to gratefully acknowledge support from the U.K. Engineering and Physical Sciences Research Council Grants No. EP/P013686/1 and No. EP/R013004/1 (C.D.O.N. and A.D.H.) and the Royal Society (P.D.C.K.) and the Leverhulme Trust (P.D.C.K. and F.M.). We also acknowledge Ph.D. studentship support from Grants No. ESPRC EP/L015110/1 (H.D.J.K.) and No. EP/K503162/1 (O.J.C.) and via the International Max-Planck Research School for Chemistry and Physics of Quantum Materials (I.M.). Computational resources provided by the U.K.'s National Supercomputer Service through the U.K. Car-Parrinello consortium (Grant No. EP/P022561/1) and by the U.K. Materials and Molecular Modelling Hub (Grant No. EP/P020194) are gratefully acknowledged. Access to the CASSIOPEE beamline (Proposal No. 20170362) at SOLEIL is also gratefully acknowledged.

[1] G. S. Pawley, W. Cochran, R. A. Cowley, and G. Dolling, Phys. Rev. Lett. **17**, 753 (1966).
[2] C. D. O'Neill, D. A. Sokolov, A. Hermann, A. Bossak, C. Stock, and A. D. Huxley, Phys. Rev. B **95**, 144101 (2017).
[3] T. Hsieh, H. Lin, J. Liu, W. Duan, A. Bansil, and L. Fu, Nat. Commun. **3**, 982 (2012).
[4] Y. Tanaka, Z. Ren, T. Sato, K. Nakayama, S. Souma, T. Takahashi, K. Segawa, and Y. Ando, Nat. Phys. **8**, 800 (2012).
[5] R. F. Brebrick, J. Phys. Chem. Solids **24**, 27 (1963).
[6] K. L. I. Kobayashi, Y. Kato, Y. Katayama, and K. F. Komatsubara, Phys. Rev. Lett. **37**, 772 (1976).
[7] L. Muldawer, J. Nonmetals **1**, 177 (1973).
[8] M. Iizumi, Y. Hamaguchi, K. F. Komatsubara, and Y. Kato, J. Phys. Soc. Jpn. **38**, 443 (1975).
[9] Y. W. Tung and M. L. Cohen, Phys. Rev. **180**, 823 (1969).
[10] P. B. Littlewood, B. Mihaila, R. K. Schulze, D. J. Safarik, J. E. Gubernatis, A. Bostwick, E. Rotenberg, C. P. Opeil, T. Durakiewicz, J. L. Smith, and J. C. Lashley, Phys. Rev. Lett. **105**, 086404 (2010).
[11] R. S. Allgaier and B. Houston, Phys. Rev. B **5**, 2186 (1972).
[12] H. T. Savage, B. Houston, and J. R. Burke, Phys. Rev. B **6**, 2292 (1972).
[13] J. R. Burke, R. S. Allgaier, B. B. Houston, J. Babiskin, and P. G. Siebenmann, Phys. Rev. Lett. **14**, 360 (1965).
[14] A. K. Okazaki, S. Wiedmann, S. Pezzini, M. L. Peres, P. H. O. Rappl, and E. Abramof, Phys. Rev. B **98**, 195136 (2018).

[15] G. Kresse and J. Furthmüller, Phys. Rev. B **54**, 11169 (1996).
[16] G. Kresse and D. Joubert, Phys. Rev. B **59**, 1758 (1999).
[17] J. P. Perdew, K. Burke and M. Ernzerhof, Phys. Rev. Lett. **77**, 3865 (1996).
[18] E. Plekhanov, P. Barone, D. Di Sante, and S. Picozzi, Phys. Rev. B **90**, 161108(R) (2014).
[19] S. Katayama and D. L. Mills, Phys. Rev. B **22**, 336 (1980).
[20] A. A. Abrikosov, Phys. Rev. B **58**, 2788 (1998).
[21] A. A. Abrikosov, Europhys. Lett. **49**, 789 (2000).
[22] X. Wang, Y. Du, S. Dou, and C. Zhang, Phys. Rev. Lett. **108**, 266806 (2012).
[23] F. Wei, X. P. A. Gao, S. Ma, and Z. Zhang, Phys. Status Solidi B **256**, 1900139 (2019).
[24] M. M. Parish and P. B. Littlewood, Nature (London) **426**, 162 (2003).
[25] A. B. Pippard, *Magnetoresistance in Metals* (Cambridge University Press, Cambridge, U.K., 1989).
[26] N. Kikugawa, A. W. Rost, C. W. Hicks, A. J. Schofield, and A. P. Mackenzie, J. Phys. Soc. Jpn. **79**, 024704 (2010).
[27] Y. Feng, Y. Wang, D. M. Silevitch, J.-Q. Yan, R. Kobayashi, M. Hedo, T. Nakama, Y. Onuki, A. V. Suslov, B. Mihaila, P. B. Littlewood and T. F. Rosenbaum, Proc. Natl. Acad. Sci. USA **116**, 11201 (2019).
[28] University of Edinburgh's Datashare repository, doi: 10.7488/ds/2931.